

LA-UR-15-20820 (Accepted Manuscript)

Design study of a laser-cooled infrared sensor

Hehlen, Markus Peter
Boncher, William Lawrence
Love, Steven Paul

Provided by the author(s) and the Los Alamos National Laboratory (2016-09-21).

To be published in: Proceedings of SPIE

DOI to publisher's version: 10.1117/12.2077846

Permalink to record: <http://permalink.lanl.gov/object/view?what=info:lanl-repo/lareport/LA-UR-15-20820>

Disclaimer:

Approved for public release. Los Alamos National Laboratory, an affirmative action/equal opportunity employer, is operated by the Los Alamos National Security, LLC for the National Nuclear Security Administration of the U.S. Department of Energy under contract DE-AC52-06NA25396. Los Alamos National Laboratory strongly supports academic freedom and a researcher's right to publish; as an institution, however, the Laboratory does not endorse the viewpoint of a publication or guarantee its technical correctness.

Design study of a laser-cooled infrared sensor

Markus P. Hehlen*, William L. Boncher, Steven P. Love

Los Alamos National Laboratory, Mailstop E549, Los Alamos, NM USA 87545

ABSTRACT

The performance of a solid-state optical refrigerator is the result of a complex interplay of numerous optical and thermal parameters. We present a first preliminary study of an optical cryocooler using ray-tracing techniques. A numerical optimization identified a non-resonant cavity with astigmatism. This geometry offered more efficient pump absorption by the YLF:10%Yb laser-cooling crystal compared to non-resonant cavities without astigmatism that have been pursued experimentally so far. Ray tracing simulations indicate that ~80% of the incident pump light can be absorbed for temperatures down to ~100 K. Calculations of heat loads, cooling power, and net payload heat lift are presented. They show that it is possible to cool a payload to a range of 90–100 K while producing a net payload heat lift of 80 mW and 300 mW when pumping a YLF:10%Yb crystal with 20 W and 50 W at 1020 nm, respectively. This performance is suited to cool HgCdTe infrared detectors that are used for sensing in the 8–12 μm atmospheric window. While the detector noise would be ~6 \times greater at 100 K than at 77 K, the laser refrigerator would introduce no vibrations and thus eliminate sources of microphonic noise that are limiting the performance of current systems.

Keywords: Solid-state optical refrigeration, cryogenic laser cooling, infrared detector, ray tracing

1. INTRODUCTION

Solid-state optical refrigeration has come a long way since its first observation by Epstein and co-workers in 1995 of cooling of an Yb^{3+} -doped fluoride glass by ~0.3 K [1]. Today, cryogenic temperatures reaching as low as 91.5 K have been achieved experimentally by pumping a 10 mol% Yb^{3+} -doped YLiF_4 crystal (YLF:10%Yb) with 50 W at 1020 nm [2]. Net heat lifts of hundreds of mW have been estimated for such a system [3]. This performance will make it possible in the near future to cool payloads such as infrared sensors to cryogenic temperatures without vibrations. A range of security, defense, non-proliferation, and science application areas will benefit from this new technology. In particular, vibration-free cryogenic cooling of space-based infrared detectors would overcome the limitations inherent to current mechanically cooled systems by eliminating sources of microphonic noise [4,5]. This may enable the much desired improvements in signal quality and thereby add significant value to space-based assets.

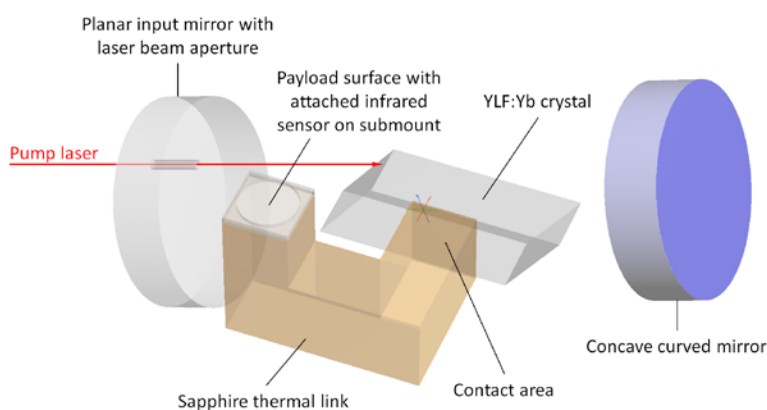


Figure 1. Conceptual representation of an optical refrigerator. The metal “clamshell” and crystal support structures are omitted for clarity.

A number of optical, thermal, and mechanical components must be integrated and optimized in order to realize a deployable laser-cooled sensor. Numerous studies have been devoted to the design and testing of the individual *hehlen@lanl.gov; phone 1 505 665-1737; www.lanl.gov

components of an optical refrigerator [3,6]. A first baseline architecture of an optical refrigerator has emerged over the past years but has not yet been fully experimentally implemented. Figure 1 shows a conceptual representation: a laser cooling-crystal such as YLF:10% Yb is placed inside a non-resonant cavity formed, for example, by a planar input mirror (left) and a curved back mirror (right). The input mirror has an aperture to admit the pump laser beam into the non-resonant cavity which allows the laser to make multiple passes through the crystal to increase the amount of absorbed pump light. The crystal is cut and aligned such that it is at Brewster’s angle with respect to the laser beam in order to minimize reflection losses. A thermal link is attached to the crystal to provide a good thermal path between the crystal and the payload while minimizing the amount of fluorescence and pump reaching and thus heating the payload. The thermal link used in this study has the shape of a rectangular waveguide with two 90° kinks and is made from sapphire, which has excellent thermal conductivity. The hypothetical payload shown here consists of a circular infrared detector bonded to a square chip carrier that is attached to the thermal link payload surface. A metal layer (not shown) can be deposited to the payload surface prior to mounting the infrared sensor assembly to act as a mirror that further reduces payload heating by fluorescence and pump light. For clarity, Figure 1 does not show the tightly-fitting metal “clamshell” structure that surrounds the crystal / thermal link assembly for the purpose of absorbing the fluorescence and pump light emanating from the assembly. Also not shown are the thin fiber supports that keep the assembly centered inside the clamshell with minimum contact area.

The device architecture shown in Figure 1 poses a significant optical design challenge. The device involves coherent pump light and incoherent fluorescence, components made from different materials and having complex shapes, multiple surfaces that can reflect, refract, and scatter, a crystal that can be birefringent, and a component layout that has to be properly aligned in three-dimensional space in order to achieve optimal performance. These optical design complexities make it necessary to utilize ray-tracing techniques to study and ultimately optimize an optical refrigerator. The present study is a first and preliminary attempt to describe an optical refrigerator using ray-tracing techniques. Our goal is to identify the key factors determining system performance and to explore computational approaches for the study of devices of this type. The thermal performance of an optical refrigerator and the associated optical parameters will be reviewed briefly in Section 2. We will then develop ray-tracing models to investigate the optical properties of the non-resonant cavity and the thermal link in Section 3. These results will then be used in Section 4 to derive estimates of payload heat lift as a function of cooling-crystal temperature and finally allow us to assess the potential performance of a laser-cooled infrared sensor.

2. THERMAL PERFORMANCE CONSIDERATIONS

At the minimum temperature of an optical refrigerator, the cooling power of the crystal, P_{cool} , is equal to the sum of all the heat loads. The latter include heating contributions from radiative (P_{rad}), conductive (P_{cond}), gaseous (P_{gas}), coating absorption (P_{coat}), and payload ($P_{payload}$) sources. The heat lift that is available in thermal equilibrium to cool a payload attached to the optical refrigerator is therefore given by

$$P_{payload} = P_{cool} - P_{rad} - P_{cond} - P_{gas} - P_{coat} \quad (1)$$

The various terms have been discussed in detail in Refs. 3 and 7, and they are briefly described in the following to define the problem. The laser-cooling power is given by

$$P_{cool} = P_{abs} \left[\eta_{ext} \frac{\alpha_r h \bar{\nu}_f}{\alpha h \nu} - 1 \right] \quad (2)$$

where P_{abs} is the pump laser power absorbed by the crystal, $\alpha = \alpha_r + \alpha_b$ is the total absorption coefficient (for a given pump wavelength λ and crystal temperature T_s) comprising both resonant (α_r) and background (α_b) absorption, η_{ext} is the external quantum efficiency of the crystal, and $h \bar{\nu}_f$ and $h \nu$ are the mean fluorescence and pump energies, respectively. The term in square brackets is the laser cooling efficiency, η_c . The load from radiative transfer of heat from the surfaces surrounding the crystal / thermal link assembly is estimated by

$$P_{rad} = \frac{\varepsilon_s A_s \sigma}{1 + \chi} (T_c^4 - T_s^4) \quad (3)$$

where $\chi = (1 - \varepsilon_c)(\varepsilon_s A_s / \varepsilon_c A_c)$, the Stefan-Boltzmann constant is $\sigma = 5.67 \times 10^{-8} \text{ W/m}^2/\text{K}^4$, ε are the thermal emissivities of the laser-cooling crystal (s) and the clamshell (c), and A are the surface areas of the laser-cooling crystal (s) and the clamshell (c). The conductive heat load through the fibers that support the assembly is given by

$$P_{cond} = \frac{N_f k_f A_f \rho_f}{d_f} (T_c - T_s) \quad (4)$$

where N_f is the total number of support fibers, k_f is the thermal conductivity of the fiber material, A_f is the cross-sectional area of one fiber, ρ_f is the fraction of A_f that is in thermal contact with the laser-cooling crystal, and d_f is the length of the fiber. The load from heat transport through the gas at low pressures is given by [8]

$$P_{gas} = \frac{a_0}{4} \left(\frac{\gamma + 1}{\gamma - 1} \right) \sqrt{\frac{2R}{\pi M}} \frac{(T_c - T_s)}{\sqrt{T_c}} pA \quad (5)$$

where R is the gas constant, p is the pressure, and $\gamma = c_p / c_v$ and M are the heat capacity ratio and the average molecular weight of the gas in the chamber, respectively. The pre-factor $a_0 = a_s a_c / [a_c + (A_c / A_s)(1 - a_c)a_s]$ contains the accommodation coefficients (a_i) for the crystal (s) and the clamshell (c) surfaces, respectively. Equation (5) is valid at the low pressures present in the vacuum chamber. Finally, absorption of fluorescence and pump light by the mirror coating on the payload interface introduces a heat load

$$P_{coat} = (1 - r)P_{opt} \quad (6)$$

where P_{opt} is the combined optical power of fluorescence and pump light incident from the thermal link onto the payload interface, and r is the reflectance of the mirror coating on the payload interface at the fluorescence and pump wavelengths.

Inspection of the various terms reveals that the available payload heat lift depends on several properties that in turn depend on the optical design. Specifically, P_{cool} involves the absorbed pump power P_{abs} which, in a simplified description, can be written as $P_{abs} = P_o(1 - e^{-\alpha L})$, where P_o is the incident pump laser power and L is the total path length of the pump laser beam in the laser-cooling crystal. L depends on the design and alignment of the non-resonant cavity; and in practice, the actual pump laser beam profile, path-dependent losses on the various interfaces, and pump rays oblique to the crystal axis pose a considerably more complex problem than the simple absorption term above suggests. P_{cool} also involves the external quantum efficiency η_{ext} , which depends on the internal quantum efficiency (η_{int}) and the escape efficiency (η_{esc}). The latter depends on the geometrical shape of the laser cooling crystal and the refractive index, and it is further complicated by reabsorption and reemission of fluorescence as well as birefringence. Similarly, the amount P_{opt} of residual fluorescence and pump light reaching the payload interface at the end of the thermal link (see Figure 1) depends on the thermal link geometry and is not easily calculated analytically. Furthermore, it depends on the fluorescence and pump power distributions at the input of the thermal link, which are a result of the non-resonant cavity design and the optical properties of the clamshell inner surfaces. Finally, surface imperfections inherent to fabricated optical components induce scattering that may or may not be significant. Ray tracing is a powerful tool to gain insight into such a complex optical system and ultimately optimize the performance of the device.

3. ANALYSIS AND OPTIMIZATION OF NON-RESONANT CAVITY AND THERMAL LINK USING RAY TRACING

3.1. Non-resonant cavity

3.1.1. Laser pumping geometry and crystal properties

The following ray-tracing calculations were carried out with the FRED Optical Engineering Software (Version 13.90.0) from Photon Engineering, LLC (Tucson, AZ). The basic setup is shown in Figure 2. The planar glass input mirror (left) had a diameter of 0.5", a thickness of 0.125", and a circular aperture with a diameter of 600 μm that was offset by 3 mm in the z -direction from the mirror center. The left side of the input mirror was uncoated while the right side had a coating with 100% reflectance. The source was defined as a laser with a wavelength of 1020 nm and having a Gaussian TEM_{00} mode profile. It was normalized to unity power and represented by 1001 sample points in both transverse directions for a total of 785,349 source rays. The laser was π -polarized with respect to the Brewster-cut input face of the downstream YLF:10%Yb crystal in order to eliminate reflection losses. The fractional transmission of a TEM_{00} beam through a circular aperture is given by $T = 1 - \exp(-2R^2/\omega^2)$, where R is the radius of the aperture and ω is the beam waist (radius to the $1/e^2$ point) [9]. A value of $\omega=198 \mu\text{m}$ was chosen to match the experimentally measured fractional laser power transmission of 99% through the 600 μm diameter aperture. The YLF:10%Yb crystal had dimensions of 11.64 mm (length) \times 4.72 mm (height) \times 3.59 mm (width) and was Brewster-cut at an angle of 55.4° . This corresponds to an index of refraction of $n = \tan(55.4^\circ) = 1.44958$ at the pump wavelength of 1020 nm, which is a good representation of the indices for birefringent YLF ($n_o = 1.448$ and $n_e = 1.470$ at 1.0 μm) calculated from published Sellmeier coefficients [10]. The birefringence of YLF was neglected for the ray-tracing calculations. The YLF:10%Yb crystal was uncoated, and no surface or bulk scattering was considered for the initial calculations. It was rotated about the x -axis by 20.8° to align the laser beam at Brewster's angle with respect to the crystal input face. We confirmed numerically that the reflection losses were indeed zero as expected for the present crystal shape and orientation. This is also evident in Figure 2 where no reflections are observed at the location where the laser beam first enters the YLF:10%Yb crystal.

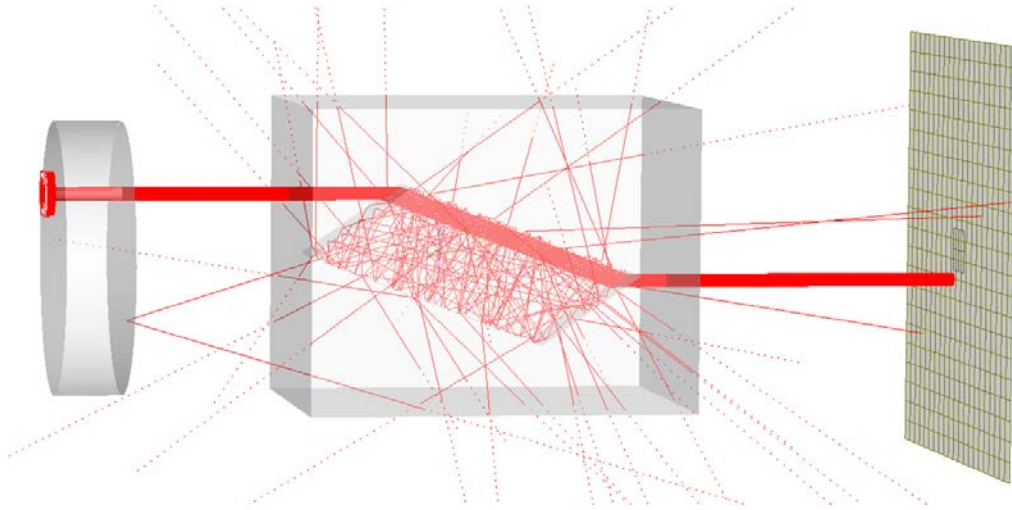


Figure 2. Basic setup of the laser source (left, red square), the planar input mirror with aperture, and the Brewster-cut YLF:10%Yb crystal. A numerical analysis surface for fluorescence (gray box) surrounded the YLF:10%Yb crystal, and a numerical analysis surface for the pump laser (olive grid) was placed downstream. An example calculation using 1961 rays to represent the laser beam is shown for illustration. Note that the pump laser induces isotropic fluorescence in the crystal.

The fluorescence spectrum of YLF:10%Yb at 100 K was taken from Ref. 11 and is shown in Figure 3. Fluorescence was implemented in the FRED software as a volume-scattering process based on the Henyey-Greenstein scattering function [12]. A pump-laser scattering event caused the wavelength to change randomly according to the luminescence spectrum (Figure 3) and the direction to change randomly to produce an isotropic power distribution. No fluorescence reabsorption and reemission processes were considered, *i.e.* only the pump light was subject to volume scattering while the fluorescence was not. The model also assumed that the Yb absorption transition remained unsaturated. The resulting

pump absorption coefficient was tuned via the mean free path (MFP) parameter in the Henyey-Greenstein volume scattering model. The resonant (pump) absorption coefficient of YLF:10%Yb at 1020 nm and 100 K was taken from Ref. 11 as $\alpha_r = 0.04 \text{ cm}^{-1}$ defined to base e . Given the crystal length of $L = 1.164 \text{ cm}$, this corresponded to a single-pass transmitted fraction of $I = I_0 e^{-\alpha_r L} = 0.9545$ (geometry of Figure 2) for normalized source power ($I_0 = 1$) and, due to the absence of pump reflections in this Brewster geometry, a single-pass absorbed fraction of 0.04549. Simulations were performed to determine the MFP that produced this absorbed fraction. For this purpose, as shown in Figure 2, the YLF:10%Yb crystal was surrounded by a numerical analysis box that recorded only the fluorescence light, and a power meter sensitive only to the pump light was placed downstream from the crystal. This allowed determination of the transmitted pump power as well as the total power of the fluorescence that escaped the YLF:10%Yb crystal. The MFP parameter in the FRED model was varied, and the resulting absorption coefficient was determined from the ray-tracing calculation (see Figure 4a). The achieved absorption coefficient and MFP are inversely related (exponent of -1.013 ± 0.009), and the pre-factor of 10.562 ± 0.493 is simply the conversion factor from units of mm (MPF) to units of cm (absorption coefficient). An MFP of 246.26 mm was predicted from the actual fit to reproduce the experimental absorption coefficient $\alpha_r = 0.04 \text{ cm}^{-1}$ of the YLF:10%Yb crystal at 1020 nm, 100 K, and for a parallel orientation of the laser polarization (\vec{E}) with respect to the crystal \vec{c} -axis. The crystallographic orientation of the YLF:10%Yb crystal however was neglected in these initial ray-tracing calculations, which likely resulted in an overestimate of the absorption coefficient because α_r is smaller for $\vec{E} \perp \vec{c}$ than for $\vec{E} \parallel \vec{c}$ polarization. Also note in Figure 4a that the laser source definition described above produced a sufficiently large number of rays that achieved relatively low statistical noise in the model data despite the low absorbance. Figure 4b confirms the expected linear relationship between the absorption coefficient and the luminescence intensity.

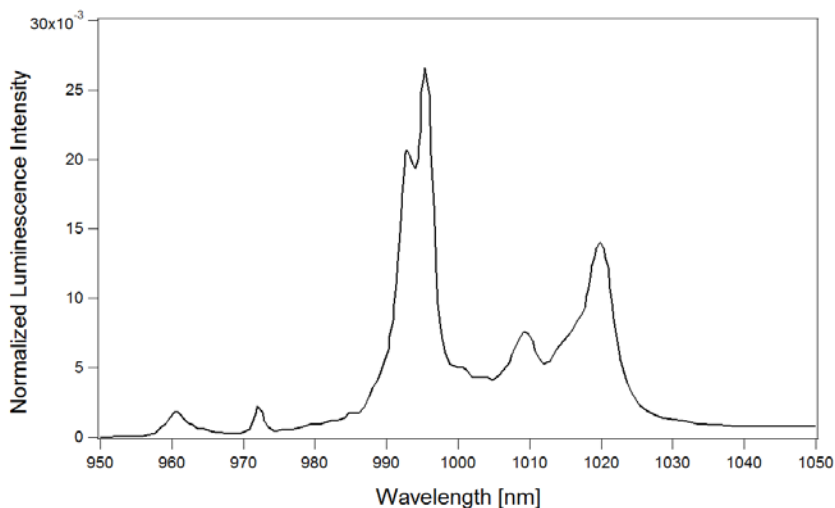


Figure 3. Fluorescence spectrum of YLF:10%Yb at 100 K (adapted from Ref. 11).

For certain bodies of high symmetry, a fraction of the luminescence will be trapped, *i.e.* totally internally reflected indefinitely [13]. In an ideal case, this light can never emerge, even in the absence of absorption. Rays on such paths were terminated in the simulations upon exceeding a certain number of internal reflections. As a result, the power of the luminescence that emerged from the crystal was less than the luminescence power generated inside the crystal (which is equal to the absorbed pump power assuming 100% *internal* quantum efficiency). The respective power ratio is the luminescence escape efficiency, η_{esc} . For this purpose, multiple calculations for different pump laser positions over a range of 3 mm in the z -direction were performed in order to account for possible position-dependence of η_{esc} . The latter varied from 78.8% to 83.3% for the various pumping positions with an average value of $(81.1 \pm 1.2)\%$, which is in good agreement with the 82.8% escape efficiency predicted analytically for a homogeneously emitting rectangular parallelepiped of $n = 1.44958$ [13]. Note again that the present calculation neither included surface scattering nor fluorescence reabsorption/reemission, both processes that would increase η_{esc} by redirecting trapped rays onto paths that can escape.

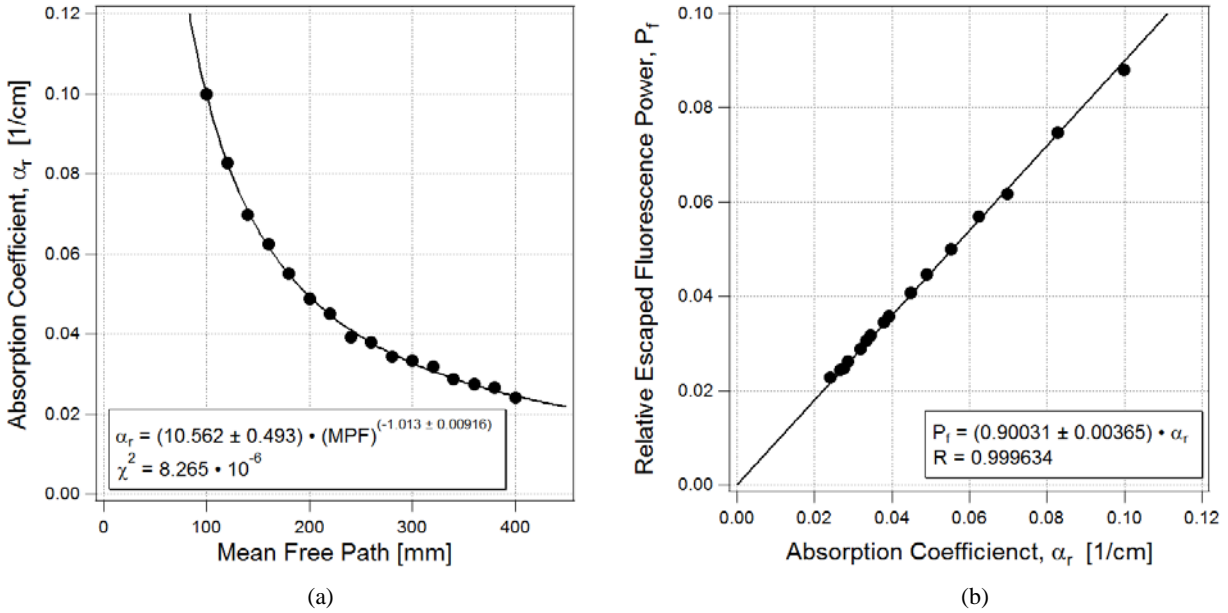


Figure 4. (a) Absorption coefficient achieved as a function of mean free path length in the FRED volume scattering model. The two quantities are inversely related, and a MFP of 246.26 mm is predicted from the fit in order to achieve $\alpha_r = 0.04 \text{ cm}^{-1}$ of YLF:10% at 1020 nm and 100 K. (b) The expected linear relationship between the power of the escaped fluorescence and the absorption coefficient is confirmed.

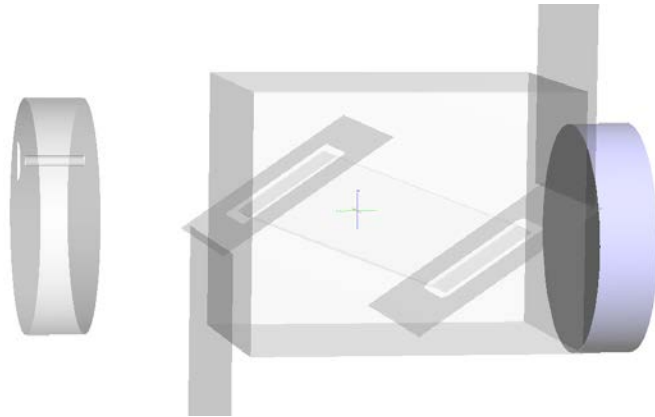


Figure 5. Basic setup of the non-resonant cavity formed by a planar input mirror with a circular aperture (left) and a curved mirror (right). The Brewster cut YLF:10%Yb crystal is placed inside the cavity. Rectangular apertures and baffles emulate the tightly fitting clamshell used in an actual optical refrigerator. The box surrounding the crystal is a virtual analysis surface for fluorescence.

3.1.2. Design and optimization of the non-resonant cavity

As shown in Figure 5, a non-resonant cavity was formed by adding a curved mirror, assumed here to have 100% reflectivity. In an actual laser-cooling device, the crystal is surrounded by a tightly-fitting and coated clamshell structure that absorbs the fluorescence and residual pump light emanating from the crystal. This geometry was computationally implemented by placing rectangular apertures at both the input and output face of the crystal (see Figure 5). The apertures were oversized to give a 1 mm gap around the crystal similar to the actual clamshell geometry. Furthermore, baffles were added above and below the apertures to block rays that intersected with the hypothetical clamshell. Both the apertures and baffles were assumed to be 100% absorbing. This simplified setup had the disadvantage that the portion of

the baffles inside the fluorescence analysis box absorbed some of the fluorescence. While this did not affect the cavity optimization, it may have resulted in an underestimate of the absorbed power in the following calculations. Work is in progress to avoid this problem by using a fluorescence analysis box that tightly surrounds the YLF:Yb crystal only.

The goal of the non-resonant cavity optimization was to maximize the fraction φ of pump power absorbed by the crystal, *i.e.* to maximize the number of pump beam passes through the crystal. This is equally accomplished by maximizing the total luminescence power emanating from the crystal, as this quantity is directly proportional to the absorbed pump power, given the assumptions of the present model. The challenge for this optimization was due to the many degrees of freedom inherent to this geometry, which in principle involved the x, y, z positions and the ϕ, φ, θ angular orientation of each mirror as well as the radius of curvature of the curved mirror. The following assumptions reduced the degrees of freedom without unnecessarily constraining the problem: (1) the mirror diameters, mirror thicknesses, mirror reflectivities, input aperture, laser source orientation, and laser beam properties remained fixed at their values described in the previous section, (2) the rotational orientation of the planar mirror was fixed to be normal to the y -axis, *i.e.* no angular adjustments were made to the planar mirror, and (3) rotation of the curved mirror about its y -axis was ignored because of the mirror's rotational symmetry. This reduced the degrees of freedom to 9. The respective parameters are summarized in Table 1 along with their notation, units, and a set of starting values. The latter were chosen as a rough approximation of the existing optical refrigerator setup at the University of New Mexico.

Table 1. Parameters of the non-resonant cavity shown in Figure 5. The table gives the starting values, the values found from a manual optimization, and the final values of a numerical optimization along with the respective total luminescence power emanating from the crystal, $F(p_1, \dots, p_9)$.

Mirror	Description	Symbol	Parameter	Starting Value	Manual Optimization	Numerical Optimization	Unit
Curved	Radius of Curvature	R	p_1	-250.0	-250.0	-243.3101	mm
	x -axis shift	Δx_c	p_2	0.0	4.4	3.9584	mm
	y -axis shift	Δy_c	p_3	-16.7	-12.365	-12.9518	mm
	z -axis shift	Δz_c	p_4	-1.7	-2.5	-2.0007	mm
	x -axis rotation	ϕ_c	p_5	0.0	-0.613	-0.5003	deg
	z -axis rotation	θ_c	p_6	0.0	0.91	-1.0041	deg
Input	x -axis shift	Δx_i	p_7	0.0	-0.29	0.9047	mm
	y -axis shift	Δy_i	p_8	0.0	5.865	4.4076	mm
	z -axis shift	Δz_i	p_9	0.0	-0.09	-0.3061	mm
$F(p)$				0.05905	0.32730	0.62324	

The total luminescence power emanating from the crystal is a function of the system parameters p_i , and it is represented by the function value $F(p_1, \dots, p_9)$ in the following calculations. We first performed a manual optimization that consisted of varying individual parameters in sequence and maximizing the fluorescence. This yielded $F(p) = 0.32730$ as an intermediate result. However, attempting to manually find the global maximum of $F(p)$ with nine degrees of freedom is a daunting task because of the presence of numerous local maxima as well as the computational effort. We therefore implemented a modified version of Powell's method [14,15] as a numerical search algorithm in an attempt to locating the global maximum of the luminescence intensity. This method was chosen because of its high computational efficiency and because it does not require knowledge of the derivatives of $F(p)$. The actual implementation was achieved as a script within the FRED software, and the algorithm was based on the respective routines described in Ref. 15. Powell's modified method is designed to search the minimum of $F(p)$, and therefore $-F(p)$ was minimized in order to find the maximum of $F(p)$. It was also necessary to implement constraints for each of the parameters in order to maintain the overall geometrical integrity of the non-resonant cavity during the numerical optimization. Table 2 summarizes the

ranges that were allowed for each of the parameter values. The algorithm only performed a calculation of $F(p)$ if all nine parameters were within their respective allowed ranges, otherwise $F(p) = 0$ was returned. The routines used the fractional tolerance, f_{tol} , as an abortion criterion for the optimization algorithm. The optimization was terminated if the function value decreased by less than f_{tol} . While a smaller f_{tol} afforded increased accuracy and ultimately yielded a greater maximum value of $F(p)$, it came at the expense of increased computational time. $f_{tol} = 0.01$ was used for most calculations while a $f_{tol} = 0.001$ was used for the final optimizations.

Table 2. Allowed ranges of parameter values used in the constrained optimization using Powell’s modified method.

Element	Description	Symbol	Parameter	Minimum Value	Maximum Value	Unit
Curved Mirror	Radius of Curvature	R	p_1	-500	-25	mm
	x -axis shift	Δx_c	p_2	-5	5	mm
	y -axis shift	Δy_c	p_3	-25	-12	mm
	z -axis shift	Δz_c	p_4	-5	5	mm
	x -axis rotation	ϕ_c	p_5	-3	3	deg
	z -axis rotation	θ_c	p_6	-3	3	deg
Input Mirror	x -axis shift	Δx_i	p_7	-3	3	mm
	y -axis shift	Δy_i	p_8	-2	-20	mm
	z -axis shift	Δz_i	p_9	-3	3	mm

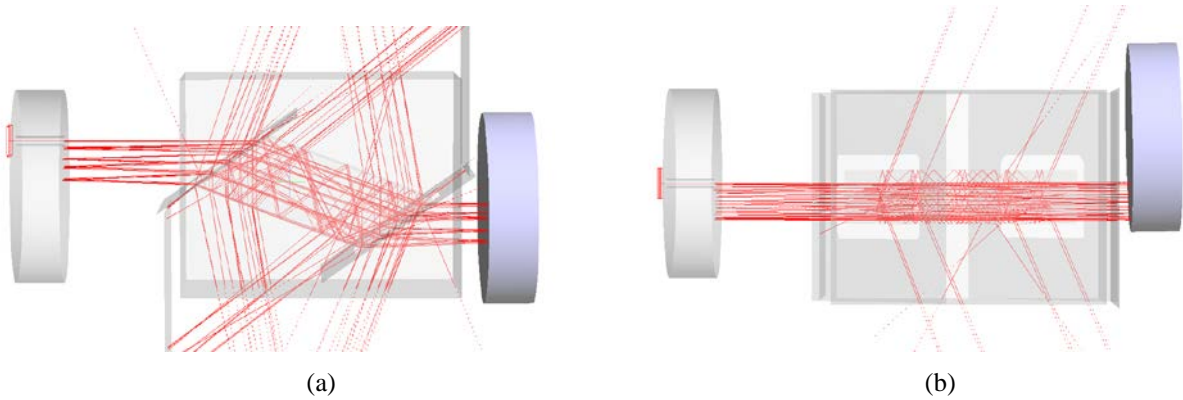


Figure 6. (a) Side view and (b) top view of the optimized non-resonant cavity having the parameters shown in Table 1. The trace of a single pump ray is shown for illustration.

Table 1 lists the best parameters obtained by the algorithm using $f_{tol} = 0.001$ and yielding the maximum luminescence power of $F(p) = 0.62324$. Using the escape efficiency of 81.1% found in the previous section and assuming 100% internal quantum efficiency, we calculate the absorbed power to be 0.76848. Given the laser power of 0.99 (relative to the source power $I_0 = 1$) launched into the non-resonant cavity, we therefore find that 77.6% of the pump power was absorbed by the YLF:10%Yb crystal in this geometry. The optimized non-resonant cavity is shown in side and top view in Figure 6. Note in Figure 6b that the periphery rather than the center of the curved mirror is used. This is one of the major differences compared to the experimental setups that have been implemented to date in which the center area of

the curved mirror was used [2]. Further studies are needed to assess the practical difficulties of aligning the cavity in this manner.

Figure 7a shows the irradiance distribution of the pump laser in close proximity to the curved mirror. The number of spots is a direct indication of the number of pump laser passes through the non-resonant cavity. The optimized geometry achieved at least 85 pump-laser passes (at least 43 spots were visible) through the non-resonant cavity. This would correspond to a path length in the YLF:10%Yb crystal of ~ 99 cm and, using the simple $P_{abs} = P_o(1 - e^{-\alpha L})$ relationship, would suggest a $\sim 98\%$ nominal pump absorption at 100 K. This is much higher than the 77.6% pump absorption calculated above. Closer inspection reveals that only $\sim 2\%$ of the pump light launched into the non-resonant cavity escapes back out the input aperture during the round trips. The remaining discrepancy is the focus of ongoing work. It may be due to pump light absorption by the clamshell, but it may also be a result of the aforementioned absorption of luminescence by the baffles. Nevertheless, the calculated 77.6% pump absorption is a lower estimate and significantly greater than the $\sim 40\%$ that has been achieved to date in actual experiments at 100 K. We speculate that one of the primary reasons for the difference is the greater number of passes and reduced pump loss from the input aperture achieved by using a laterally shifted and tilted curved mirror in the present optimized geometry (see Figure 6b). The pump absorption may also have been overestimated by neglecting saturation of the Yb^{3+} absorption.

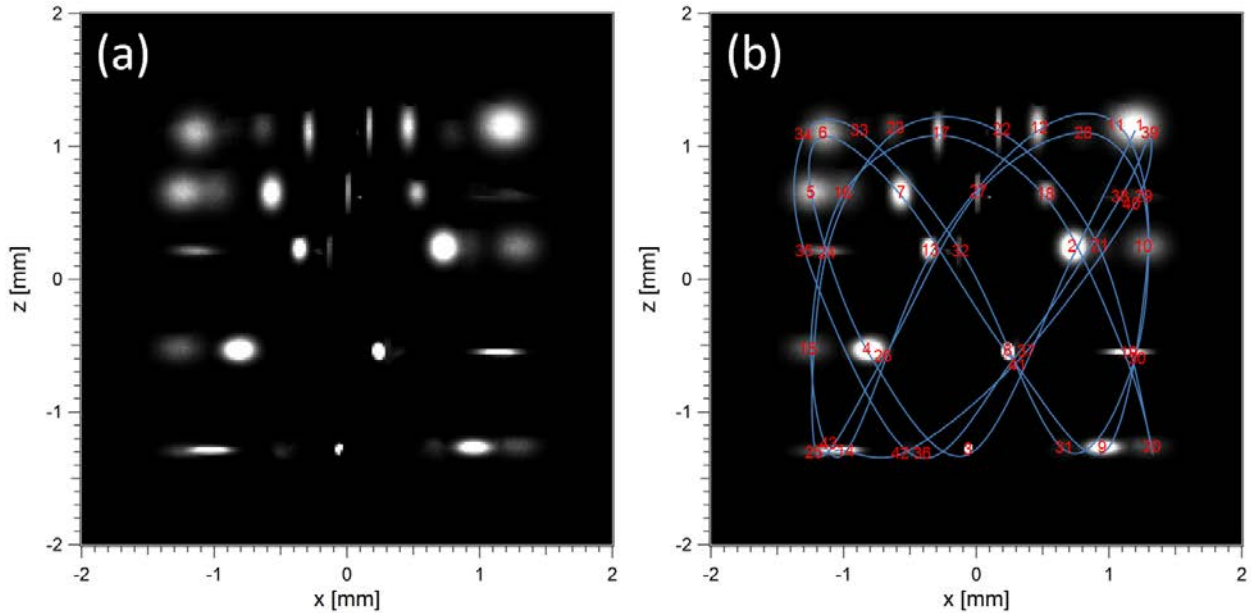


Figure 7. (a) Pump irradiance distribution on a hypothetical detector plane placed in proximity and parallel to the curved mirror. (b) The sequence of spots on this plane as the pump laser propagates in the non-resonant cavity is indicated by red numbers and connected by a spline that reveals a Lissajous-type curve.

Figure 7a shows that the pump-laser spots are arranged in rows on the curved mirror. Connecting the spots in sequence as the pump laser propagates in the non-cavity reveals a Lissajous-type curve that is overlaid on the pump-laser spots in Figure 7b. Such propagation patterns are a common feature of non-resonant cavities [16]. The spot pattern produced in a non-resonant cavity without astigmatism is circular or ellipsoidal in shape. In contrast, spot patterns on Lissajous or skewed Lissajous curves form upon the introduction of simple or general astigmatism in the mirrors, respectively. Thus, the circular (Herriott type) pump-spot patterns observed in laser-cooling cavities studied to date are a result of using the center portion of the spherical curved mirror. In contrast, the geometry found in this study (Table 1) used a square area off-axis on the tilted spherical mirror, thereby inducing some degree of simple astigmatism and producing a Lissajous pattern on the curved mirror. This astigmatism is evident in Figure 7a from the spots alternating between vertically and horizontally oriented foci as the laser propagates through the non-resonant cavity.

Having identified a favorable cavity geometry for the crystal at 100 K, we are now in a position to predict the absorbed power for other temperatures. Let us neglect the temperature dependence of the crystal refractive index and assume the resonant absorption coefficient α_r to be the only temperature dependent parameter. Figure 8 (right axis) shows α_r in YLF:10%Yb for different temperatures [7] along with an interpolation. The absorbed fraction φ calculated for the optimized cavity geometry defined in Table 1 is presented in Figure 8 (left axis) for different temperatures. Two features are particularly noteworthy. First, the cavity allows for a nearly constant absorbed fraction of $\sim 81\%$ in the 100 – 300 K range even though α_r varies by a factor of ~ 13 . This is a result of the extended path length that is possible in this well-aligned cavity. As the temperature decreases, the decreasing α_r is offset by an increasing number of pump passes through the crystal. Second, a sharp drop of the absorbed fraction is predicted for temperatures < 100 K, which will make it difficult to achieve significant heat lifts in this regime using this particular system. As noted above, the magnitude of the absorbed fraction may be underestimated in this calculation.

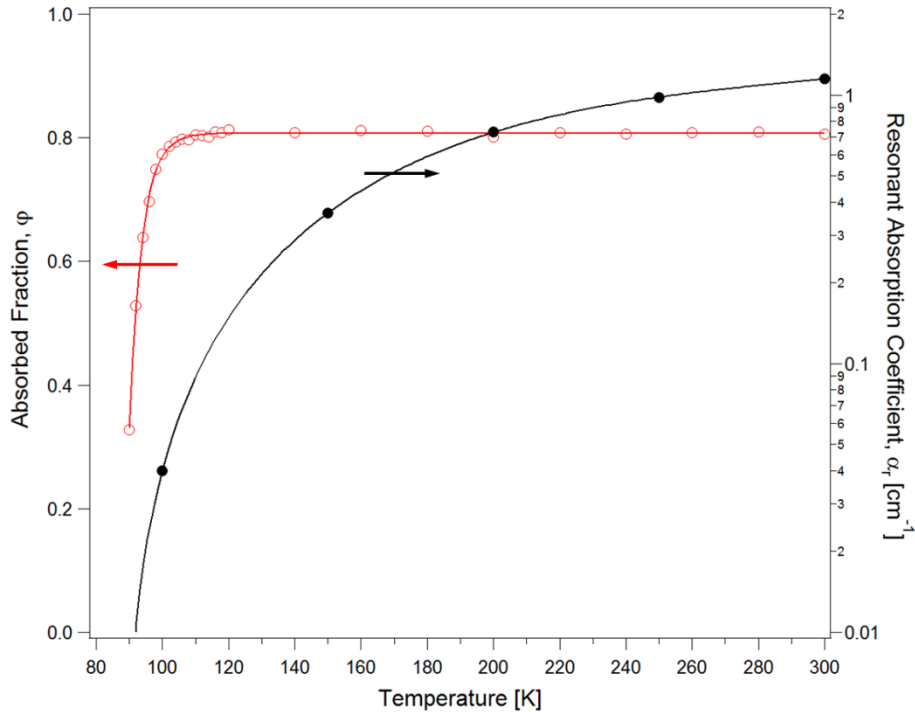


Figure 8. *Right axis:* Resonant absorption coefficient of YLF:10%Yb at different temperatures (adapted from Ref. 7); the interpolation line is fit to a 4th degree polynomial. *Left axis:* Fraction of pump power absorbed by the YLF:10%Yb crystal inside the cavity geometry defined by Table 1; the interpolation line is fit to the function $y = a + (a - b)/\{1 + (c/x)^d\}$.

3.2. Thermal Link

In an optical refrigerator, the laser-cooling crystal and the payload must be connected by a thermal link that provides a good thermal path between the crystal and the payload while preventing luminescence emitted by the crystal to reach and thus heat the payload. One way this can be accomplished is by means of a kinked rectangular waveguide [17] as shown in Figure 1. Such a waveguide can be fabricated from sapphire and be diffusion bonded directly to the YLF:Yb crystal to eliminate any adhesives that might absorb pump light and fluorescence and thus heat. A mirror coating can be applied to the payload surface to reflect any residual pump light and luminescence and thus further reduce the heat load onto a payload attached to this surface.

In this section we will perform ray-tracing simulations of this particular thermal link design to assess its effectiveness in rejecting pump light and luminescence from reaching the payload. Our initial goal was to define an assembly in the FRED software consisting of the YLF:10%Yb crystal and the thermal link, and then simulate its performance inside the cavity that was optimized in Section 3.1. However, a challenge was encountered in defining this assembly in the FRED

software. FRED defines objects as a set of surfaces that enclose a volume, and each surface is defined by the two materials it separates. In that sense, there is strictly no inside or outside of an object, rather the rays just traverse surfaces from one material into another. Simply joining the rectangular surface of the thermal link to one side of the YLF:10%Yb crystal was not possible because the thermal link only partially covered this crystal surface. Rays being transmitted from within the crystal across this surface could therefore enter either the thermal link or the surrounding air, creating an ambiguity in the emergent material. This issue will be addressed in further studies, however a simpler approach was taken here. Rather than attaching the thermal link to the crystal in the model, we first defined an analysis surface on the crystal in the thermal link contact area as shown in Figure 9 (top). The analysis surface allowed us to determine both the power and the angular distribution of rays incident from the YLF:10%Yb crystal on this surface and, by knowledge of the refractive indices, the power and angular distribution of rays emerging into the sapphire thermal link. This information was then used to define an appropriate light source that allowed us to simulate the thermal link separately from the crystal and cavity. We found that the 4 mm × 5 mm contact area of the thermal link intercepted a total power of 3.003×10^{-2} (relative to the source power $I_0 = 1$), which consisted of 86.3% luminescence and 13.7% pump light. Figure 9 shows both the irradiance and angular distribution of the rays incident on the thermal link contact surface. The angular distribution is approximately Lambertian. Assuming the incident rays to be unpolarized and assuming an average refractive index of sapphire of 1.7527 at 1020 nm, we found that the transmittance from YLF:Yb to sapphire is 0.9715, *i.e.* the relative power injected from the YLF:Yb crystal into the thermal link through the contact area was 2.947×10^{-2} .

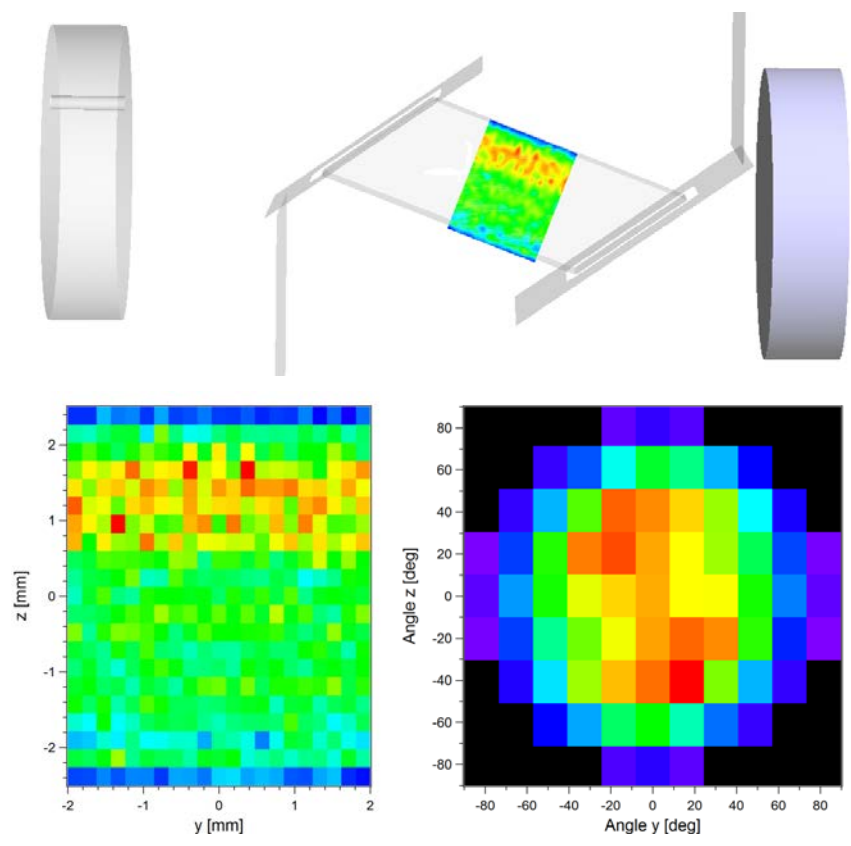


Figure 9. *Top*: Total irradiance distribution on YLF:10%Yb crystal surface in the thermal link contact area. *Bottom*: Spatial (left) and angular (right) irradiance distribution over the thermal link contact area.

The non-uniform irradiance distribution at the thermal link input (see Figure 9) was ignored in the following, and the calculation assumed a random spatial distribution of rays with a Lambertian angular distribution and a power of 2.947×10^{-2} at the input surface of the thermal link. We found a total power of 6.445×10^{-6} reaching the payload surface from within the thermal link, and the respective irradiance distribution is shown in Figure 10. Thus, the thermal link

achieved a $\sim 4500\times$ rejection of the incident light. Assuming a 50 W pump laser, this would correspond to 0.322 mW of residual luminescence and pump light incident on the payload surface. This heat load could be further reduced by adding a mirror to the payload surface. For example, a silver mirror having a reflectance of 97% around $1\ \mu\text{m}$ would reduce the heat load on the payload to a rather insignificant $\sim 10\ \mu\text{W}$.

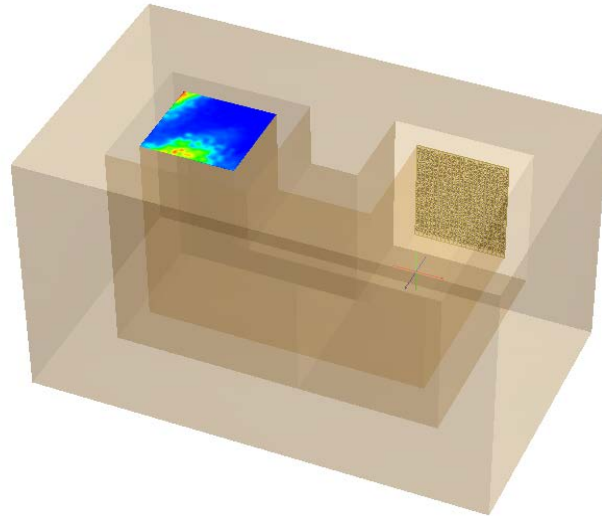


Figure 10. Rectangular sapphire thermal link with two 90° kinks surrounded by a clamshell at distance of 1 mm from all surfaces. Light is injected from the back surface. The irradiance distribution on the payload surface (top) is shown.

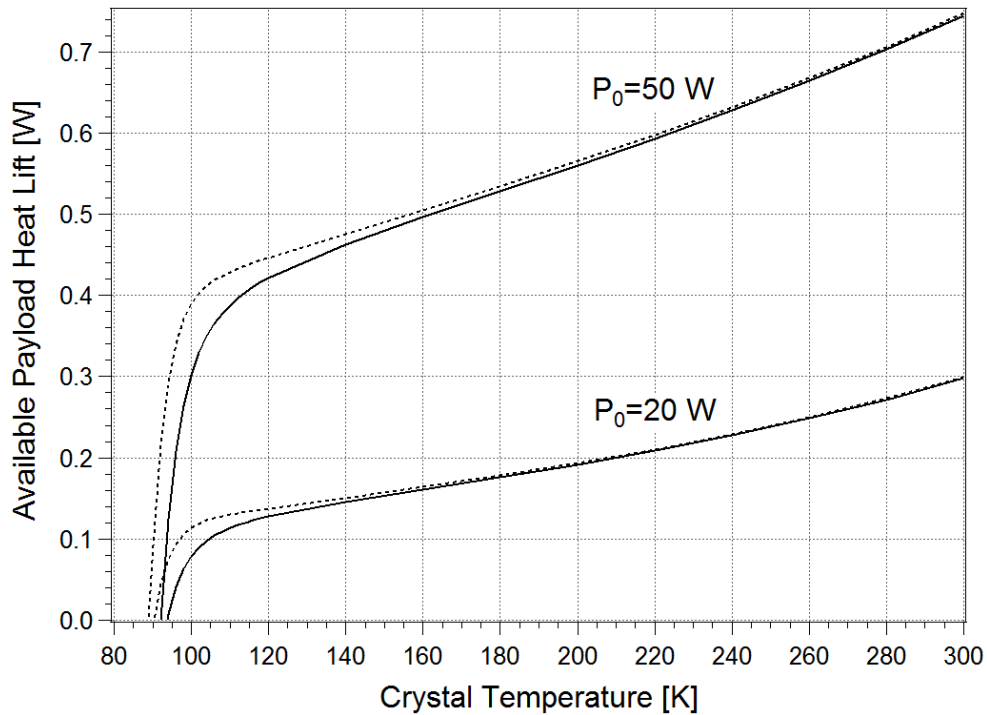


Figure 11. Calculated available payload heat lifts (in thermal equilibrium) as a function of crystal operating temperature for two different incident pump powers. The solid lines are for a background absorption coefficient of an existing YLF:10%Yb crystal ($\alpha_b = 10^{-4}\ \text{cm}^{-1}$, see Table 3) while the dotted curves are for a hypothetical purer crystal having $\alpha_b = 10^{-5}\ \text{cm}^{-1}$.

4. THERMAL PERFORMANCE CALCULATIONS

The results of the ray-tracing study of Section 3 can now be incorporated into the thermal model presented in Section 2 with the goal of estimating the heat lift that is available to cool a payload attached to the thermal link. The present work advances a basic model published earlier [3]. Table 3 summarizes the various thermal, optical, and geometric parameters used to calculate heat loads in Eqs. (1)–(6) for the optimized system defined in Figure 1 and Table 1. The clamshell surrounding the assembly was assumed to have its inside surfaces coated with a solar-selective coating (such as Maxorb™) and placed at a distance of 1 mm. The clamshell had two rectangular apertures for the pump (see Figure 5) and a square aperture for the thermal link payload interface (see Figure 10). The thermal emissivity of the clamshell was estimated as $\varepsilon_c = 0.202$ by taking the weighted sum of the surfaces coated with Maxorb™ ($\varepsilon = 0.08$ over 723 mm^2) and the apertures open to the outside ($\varepsilon = 1$ over 111 mm^2). We assumed that the assembly was held in place by 18 silica fiber supports, *i.e.* 3 fibers each from 6 directions. The calculations further assumed the clamshell to be held at 300 K. The properties of the crystal are for a recent sample of YLF:10%Yb that achieved a measured low background absorption of $\alpha_b = 1 \times 10^{-4} \text{ cm}^{-1}$ and a high external quantum efficiency of $\eta_{ext} = 0.998$. The temperature dependence of the mean fluorescence energy was taken from Ref. 7.

Table 3. Parameters used for the heat lift estimates for an optical cryocooler using a YLF:10%Yb³⁺ crystal.

Parameter	Symbol	Value	Units	Notes
Crystal temperature	T_s	Variable	K	see text
Clamshell temperature	T_c	300	K	
Crystal + thermal link area	A_s	605×10^{-6}	m ²	Design of Figure 1
Clamshell area	A_c	723×10^{-6}	m ²	see text
Accommodation coefficients	a_i	1		Ref. 8
Molecular weight of residual gas	M	0.02897	kg/mol	Air
Heat capacity ratio of gas, c_p/c_v	γ	1.4		
Chamber pressure	P	1×10^{-5}	Torr	
Crystal-clamshell distance	d	1×10^{-3}	m	
Number of support fibers	N_f	18		
Support fiber diameter	d_f	500×10^{-6}	m	
Support fiber thermal conductivity	k_f	1.38	W/(m K)	Fused silica, assumed temperature independent
Fractional contact area	δ_A	0.01		
Thermal link coating reflectance	r	0.97		Silver, assumed temperature independent
Crystal thermal emissivity	ε_s	0.80		assumed temperature independent
Clamshell effective thermal emissivity	ε_c	0.202		assumed temperature independent, see text
Yb ³⁺ concentration in YLF		10	mol%	with respect to yttrium
Background absorption coefficient	α_b	1×10^{-4}	cm ⁻¹	assumed temperature independent
Pump wavelength	λ_p	1020	nm	
External quantum efficiency	η_{ext}	0.998		assumed temperature independent
Incident pump laser power	P_0	variable	W	see text
Absorbed fraction	ϕ	calculated		see Sect. 3.2.2, Figure 8

The thermal calculations give insight into the relative importance of the various heat loads onto the crystal / thermal link assembly. At 100 K and $P_0 = 50 \text{ W}$, we find a total heat load of 70.2 mW in which the radiative term of Eq.(3) dominates with 85.8%, followed by the conductive term of Eq.(4) with 13.9%. Heat load through the gas [Eq.(5)] only accounts for 0.3%, and heating from light absorbed by the payload mirror coating is found to be negligible. The greatest potential for improvements in the optical cryocooler design is therefore expected from optimizing the clamshell geometry and coating as well as minimizing the heat load from the crystal / thermal link support structure. A cooling power of $P_{cool} = 372.3 \text{ mW}$ was calculated for this temperature and pump power, thus leaving $P_{payload} = 302.1 \text{ mW}$

of heat lift for the payload in thermal equilibrium [Eq.(1)]. Figure 11 shows the result of evaluating Eq.(1) with the parameters of Table 3 over a range of temperatures for both 20 W and 50 W of incident pump power. This result illustrates the tradeoff between the cooling temperature and the available payload heat lift. Without a payload, this system is expected to cool to ~ 93 K. Payloads having heat loads of < 300 mW are expected to cool to < 100 K using 50 W of incident pump power. A $10\times$ purer crystal ($10\times$ smaller α_b) would slightly reduce the minimum temperature, however it would offer $\sim 30\%$ greater heat lift at 100 K.

These results are relevant in particular for HgCdTe infrared detectors, which are used for sensing radiation in the 8–12 μm atmospheric window and which must ideally be cooled to liquid nitrogen temperature. The dark current, I_d , of a HgCdTe detector for 12 μm ($E_g \approx 0.1$ eV) is $\sim 36\times$ greater at 100 K than at 77 K, a typical operating temperature of such sensors. The detector noise, which arises from statistical fluctuations in the dark current and scales as $\sqrt{I_d}$, is $\sim 6\times$ greater at 100 K than at 77 K. This performance may be acceptable for many applications, particularly as it comes with the critical advantages of vibration-free and reliable operation that are inherent to a solid-state refrigerator. The associated engineering tradeoffs however are complex and will depend on the specifics of the system.

5. CONCLUSIONS

The design and optimization of a solid-state optical refrigerator has to take into account a complex interplay of numerous optical and thermal parameters. We have shown ray tracing to be a valuable tool for calculating the pump power that is absorbed by the laser-cooling crystal as a function of the optical system geometry as well as temperature. Preliminary results of a first study were presented, and they should be viewed as initial estimates. Many of the assumptions and simplification made in this first model are the subject of ongoing studies, including the proper inclusion of the clamshell and crystal / thermal link geometry, the effects of birefringence and scattering, the impact of a changing pump polarization, the analysis of volume excitation density and saturation of the Yb^{3+} transition, and the proper treatment of reabsorption / reemission processes. Combined, these aspects will likely change some of the quantities presented in this preliminary study.

The preliminary results however offer first valuable insights. A numerically optimized non-resonant cavity with astigmatism achieved more efficient pump absorption than what has been achieved experimentally in non-resonant cavities without astigmatism. Calculations indicated that $\sim 80\%$ of the pump light is absorbed for temperatures down to ~ 100 K. This has allowed us to calculate both the laser-cooling power and the various heat loads. Of the latter, radiative and conductive heat loads dominated, suggesting the areas where most improvements could be made. In particular, studying the tradeoff between a double kinked thermal link with excellent light rejection but large area versus a single kinked thermal link with less efficient light rejection but smaller area should be conducted. We expect that it is possible to cool a payload to a range of 90–100 K while producing a net payload heat lift of 80 mW and 300 mW when pumping with 20 W and 50 W, respectively. This performance may be suited to cool HgCdTe infrared detectors used for sensing in the 8–12 μm atmospheric window. While the detector noise would be $\sim 6\times$ greater at 100 K than at 77 K, the laser refrigerator would introduce no vibrations and thus eliminate sources of microphonic noise that are limiting current systems.

ACKNOWLEDGMENTS

We gratefully acknowledge the support of the U.S. Department of Energy through the LANL Laboratory Directed Research & Development Program for this work. MPH is grateful for many fruitful discussions with Seth D. Melgaard (Department of Physics & Astronomy, University of New Mexico, Albuquerque, NM) and Air Force Research Laboratory, Kirtland AFB, Albuquerque, NM) and Richard I. Epstein (CryoRay Coolers, Santa Fe, NM).

REFERENCES

- [1] Epstein, R.I., Buchwald, M.I., Edwards, B.C., Gosnell, T.R., Mungan, C.E., “Observation of laser-induced fluorescent cooling of a solid,” *Nature* 377, 500-503 (1995).

- [2] Melgaard, S.D., Seletskiy, D.V., Albrecht, A.R., Sheik-Bahae, M., "Optical refrigeration demonstrates the first cooling below 100 K," Paper 9380-1, Laser Refrigeration of Solids VIII, SPIE Photonics West OPTO, San Francisco, CA, February 2015.
- [3] Epstein, R.I., Hehlen, M.P., Sheik-Bahae, M., Melgaard, S.D., "Optical cryocoolers for sensors and electronics," Proc. SPIE 9070, 90702K-1 (2014).
- [4] Gilmore, G. and Hemingway, J.D., [Practical Gamma-Ray Spectrometry], John Wiley & Sons Inc., New York (1998).
- [5] Veprik, A.M., Babitsky, V.I., Pundak, N., Riabzev, S.V., "Suppression of cryocooler-induced microphonics in infrared imagers," Cryogenics 49, 449-454 (2009).
- [6] Hehlen, M.P., Sheik-Bahae, M., Epstein, R.I., "Solid-state optical refrigeration," in *The Handbook on the Physics and Chemistry of Rare Earths* 45, 179-260 (2014).
- [7] Melgaard, S.D., "Cryogenic optical refrigeration: Laser cooling of solids below 123 K," Ph.D. dissertation, University of New Mexico, Albuquerque, NM, USA, (2013).
- [8] White, G.K., "Experimental techniques in low-temperature physics," Clarendon Press, Oxford (1979).
- [9] Uehara, K. and Kikuchi, H., "Transmission of a Gaussian beam through a circular aperture," Appl. Opt. 25, 4514-4516 (1986).
- [10] Barnes, N.P. and Gettemy, D.J., "Temperature variation of the refractive indices of yttrium lithium fluoride," J. Opt. Soc. Am. 70, 1244-1247 (1980).
- [11] Melgaard, S., Seletskiy, D., Sheik-Bahae, M., Bigotta, S., Di Lieto, A., Tonelli, M., Epstein, R., "Spectroscopy of Yb-doped YLF crystals for laser cooling," Proc. SPIE 7614, 761407 (2010).
- [12] Henyey, L.C. and Greenstein, J.L., "Diffuse radiation in the galaxy," Astrophys. J. 93, 70-83 (1941).
- [13] Shurcliff, W.A., and Jones, R.C., "The trapping of fluorescent light produced within objects of high geometrical symmetry," J. Opt. Soc. Am. 39, 912 (1949).
- [14] Acton, F.S., "Numerical methods that work," Harper & Row, New York, NY, pp. 464-467 (1970).
- [15] Press, W.H., Flannery, B.P., Teukolsky, S.A., Vetterling, W.T., "Numerical Recipes – The art of scientific computing," Cambridge University Press. New York, NY, Chapter 10 (1986).
- [16] Paul, J.B., Lapson, L., Anderson, J.G., "Ultrasensitive absorption spectroscopy with a high-finesse optical cavity and off-axis alignment," Appl. Opt. 40, 4904-4910 (2001).
- [17] Parker, J., Mar, D., Von der Porten, S., Hankinson, J., Byram, K., Lee, C., Mayeda, M.K., Haskell, R., Yang, Q., Greenfield, S., Epstein, R., "Thermal links for the implementation of an optical refrigerator," J. Appl. Phys. 105, 013116 (2009).